Check for updates

ADVANCED MATERIALS
www.advmat.de

Ultrathin PtPd-Based Nanorings with Abundant Step Atoms Enhance Oxygen Catalysis

*Yingjun Sun, Xu Zhang, Mingchuan Luo, Xu Chen, Lei Wang, Yingjie Li, Mingqiang Li, Yingnan Qin, Chunji Li, Nuoyan Xu, Gang Lu, Peng Gao, and Shaojun Guo**

The lack of highly active and stable catalysts with low Pt usage for the oxygen reduction reaction (ORR) is a major barrier in realizing fuel cell-driven transportation applications. A general colloidal chemistry method is demonstrated for making a series of ultrathin PtPdM (*M* = Co, Ni, Fe) nanorings (NRs) for greatly boosting ORR catalysis. Different from the traditional ultrathin nanosheets, the ultrathin PtPdM NRs herein have a high portion of step atoms on the edge, high Pt utilization efficiency, and strong ligand effect from M to Pt and fast mass transport of reactants to the NRs. These key features make them exhibit greatly enhanced electrocatalytic activity for the ORR and the oxygen evolution reaction (OER). Among all the PtPdM NRs, the PtPdCo shows the highest ORR mass and specific activities of 3.58 A mg^{-1} and 4.90 mA cm^{-2} at 0.9 V versus reversible hydrogen electrode (RHE), 23.9 and 24.5-fold larger than those of commercial Pt/C in alkaline electrolyte, respectively. The theoretical calculations reveal that the oxygen adsorption energy (E_O) can be optimized under the presence of step atoms exposed on the edge and ligand effect induced by Co. They are stable under ORR conditions with negligible changes after 30 000 cycles.

Polymer electrolyte membrane fuel cells are considered to be essential in closing the hydrogen energy cycles due to their high efficiency in energy conversion.[1–4] However, the unaffordable usage of precious metal platinum as the electrocatalyst to drive the sluggish oxygen reduction reaction (ORR) at cathode largely hinders its commercialization.[5–7] To overcome this limitation, vast efforts have been devoted to boosting the ORR activity with high Pt utilization efficiency and high intrinsic turnover frequency by means of forming alloys, tuning morphologies, manipulating architectures, optimizing supports, and so on.[8–18] In spite of the considerable progress, an activity gap to achieve the commercialization still remains, which thus necessitates further optimization of catalytic nanostructures based on the understanding of structure-performance relationship.[19,20]

Recently, ultrathin 2D Pt-based multimetallic nanocrystals with the thickness of a few atomic layers have shown impressive performance for heterogeneous catalysis due to their high exposure of atoms and feasibility of surface modification.[21–25] In explaining the remarkable catalytic performance of ultrathin nanosheets, the widely and intuitively accepted viewpoint is that the top/bottom (111) facets, accounting for almost 90% of

Y. Sun, Dr. M. Luo, Dr. Y. Li, Y. Qin, Dr. C. Li, N. Xu, Prof. S. Guo
Department of Materials Science & Engineering
College of Engineering
Peking University
Beijing 100871, China
E-mail: guosj@pku.edu.cn

Y. Sun, Y. Qin, Prof. L. Wang
College of Chemistry and Molecular Engineering
Qingdao University of Science and Technology
Qingdao 266042, China

Prof. X. Zhang, Prof. G. Lu
Department of Physics and Astronomy
California State University
Northridge, CA 91330, USA

Prof. X. Chen
State Key Laboratory of Chemical Resource Engineering
Beijing University of Chemical Technology
Beijing 100029, China

The ORCID identification number(s) for the author(s) of this article can be found under https://doi.org/10.1002/adma.201802136.

DOI: 10.1002/adma.201802136

M. Q. Li, Prof. P. Gao
Electron Microscopy Laboratory
and International Center for Quantum Materials
School of Physics
Peking University
Beijing 100871, China

Prof. P. Gao
Collaborative Innovation Centre of Quantum Matter
Beijing 100871, China

Prof. S. Guo
BIC-ESAT
College of Engineering
Peking University
Beijing 100871, China

Prof. S. Guo
Department of Energy and Resources Engineering
College of Engineering
Peking University
Beijing 100871, China

Prof. S. Guo
Beijing Key Laboratory for Magnetoeletric Materials
and Devices (BKL-MEMD)
Peking University
Beijing 100871, China

 © 2018 WILEY-VCH Verlag GmbH & Co. KGaA, Weinheim

the surface atoms, are the key in enhancing ORR activity.[26–31] However, it is still unknown whether the edges, accounting for only a small fraction of surfaces of nanosheets, can promote or delay the reaction rates. To the best of our knowledge, there is no report that specifically addresses this open problem because the construction of an ultrathin 2D nanomaterial with atoms on the edges rather than top/bottom facets is still a grand challenge.

Considering the atoms located at steps, ledges, and kinds of high-indexed facets are intrinsically very active, herein we report a universal method for the controlled synthesis of ultrathin hexagonal PtPd-based multimetallic nanorings (NRs), in which the step atoms dominate the surface, as highly efficient bifunctional electrocatalysts for enhancing ORR and oxygen evolution reaction (OER). The systematic mechanism studies reveal that the existence of carbonyl group in the synthetic system played an essential role in forming 2D nanoplate structure, whereas the presence of moderate bromide ion and dissolved oxygen (Br^-/O_2) is the key in obtaining 2D NRs structure. The present strategy is highly universal for making various types of ultrathin bimetallic and multimetallic PtPdM (M = Co, Ni, Fe) alloyed NRs. These 2D ultrathin PtPdM NRs possess high atom utilization, high portion of step atoms, and strong ligand effect from M to Pt, making them display unexpected bifunctional properties toward ORR and OER. Among all the multimetallic NRs, the 2D PtPdCo NRsshow the highest specific activity of 4.90 mA cm^{-2} and mass activity of 3.58 A mg^{-1} for ORR at 0.9 V versus reversible hydrogen electrode (RHE), better than those of the PtPd NRs and Ni- or Fe-alloyed PtPd NRs, and also 24.5 and 23.9 higher than those of the commercial Pt/C. Density function theory (DFT) calculations reveal that the presence of the step atom on the edge of NRs and the ligand effect induced by alloying Co can optimize oxygen adsorption energy (E_O), promoting the ORR activity. Meanwhile, they are very stable for ORR by showing almost no changes in polarization curves and metal composition after 30 000 cycles. In particular, 2D PtPdCo NRs also present high OER activity with an onset potential of ≈1.5 V versus RHE and a high turnover frequency (TOF) of 0.14 s^{-1} at the potential of 300 mV, much better than those of PtPd NRs and commercial Pt/C.

The 2D PtPdM NRs (M = Co, Ni, Fe) were made in non-aqueous conditions by using platinum II) acetylacetonate ($Pt(acac)_2$), palladium II) acetylacetonate ($Pd(acac)_2$), and acetylacetonate compound $M(acac)_x$, such as $Co(acac)_3$, $Ni(acac)_2$, $Fe(acac)_3$, as the metal precursors, tungsten carbonyl ($W(CO)_6$) and ammonium bromide (NH_4Br) as the structure-directing agents, oleylamine as the solvent. These chemicals were added into a vial, and ultrasonicated to get a homogeneous solution (see details in Supporting Information). The mixture was then heated at room temperature to 150 °C for 5 h in an oil bath. The obtained black product was collected by centrifugation and washed with cyclohexane after it was cooled to room temperature.

The morphology and structure of the as-made 2D PtPdM NRs were characterized by transmission electron microscopy (TEM), high-angle annular dark-field scanning TEM (HAADF-STEM), high-resolution TEM (HRTEM) and atomic force microscopy (AFM). Using PtPdCo NRs as an example, the hexagonal nanorings were the dominant products from the representative HAADF-STEM and TEM images (**Figure 1**A and Figure S1, Supporting Information). The average edge length is 27.4 nm, ≈5–6 atomic layer width, determined by measuring around 100 randomly selected NRs. High-magnification STEM image reveals that the surface of NR edge is not smooth (Figure 1B). The thickness of PtPdCo NRs is determined to be 1.8 nm by AFM image (Figure S2, Supporting Information), also confirmed by analyzing the NRs vertical on the TEM grid (Figure S3, Supporting Information). Powder X-ray diffraction (PXRD) pattern of the PtPdCo NRs shows they employ a face-centered cubic (*fcc*) structure. The main diffraction peaks of PtPdCo are located between those of *fcc* Pt (JCPDS No. 04–0802) and *fcc* Pd (JCPDS No. 46–1043) along with a slightly positive shift compared to those of PtPd NRs, suggesting the formation of PtPdCo alloys (Figure 1C and Figure S4, Supporting Information). From the X-ray photoelectron spectroscopy analysis, the chemical state of Co in PtPdCo NRs surface is a mixture of oxidized Co^{2+} and metallic Co (Figure S5, Supporting Information). Notably, the existence of Co^{2+} in Pt-based alloyed catalysts usually happens because the surface Co can be oxidized easily.[32,33] The composition of Pt/Pd/Co in NRs is estimated to be 47/41/12 by the TEM energy-dispersive X-ray spectroscopy (TEM-EDS) (Figure 1D), in line with the result from inductively coupled plasma-atomic emission spectroscopy (ICP-AES, 48/41/11). The STEM-EDS elemental mapping of a single PtPdCo NR indicates the distribution of Pt, Pd, and Co in the NR (Figure 1E). The EDS line scan image shows the three element (Pt/Pd/Co) traces have very good matching with two peaks at the edges and one valley in the center (Figure S6, Supporting Information). The HRTEM images along the [112] zone axis taken from an individual nanoring further confirm the edges of NR contain abundant step atoms (Figure 1F,G and Figure S7, Supporting Information). The lattice spacing of PtPdCo NRs is 0.223 nm, slightly lower than that of the (111) plane of *fcc* Pt or Pd. By analysis of the fast Fourier transform (FFT) pattern in the inset of Figure 1G, we can determine that the step atoms are dominated by the (311) high-index facets.

The synthesis of 2D nanorings was a great challenge due to the intrinsically isotropic growth behavior of metals. Therefore, we investigated the morphologies, composition and structure of PtPdCo NRs at different reaction times during the synthesis through TEM (**Figure 2**A–D), ICP-AES (Figure 2E) and PXRD (Figure 2F). The product collected after 1 min reaction was dominated by many ultrathin nanoplates (Figure 2A). ICP-AES results reveal that the nanoplates were mainly composed of Pd atoms (81%), implying the preferential reduction of Pd precursor at initial stage. Owing to selective adsorption of Br^- ions on the side facet,[34] the newly formed Pd atoms were expected to diffuse onto the top and bottom surfaces. The Pd atoms around the periphery of the Pd nanoplate have not enough time to migrate to the interior part of the Pd nanoplates. Therefore, the nanoplates have a thicker periphery but a thinner interior part. As a control, the sample produced by the reaction without the existence of Pt precursors also showed the similar phenomenon (Figure S8, Supporting Information). Therefore, higher contrast between the edge and interior (Figure 2B), and the increased Pt percentages (Figure 2E) were

© 2018 WILEY-VCH Verlag GmbH & Co. KGaA, Weinheim

15214095, 2018, 38, Downloaded from https://onlinelibrary.wiley.com/doi/10.1002/adma.201802136 by Peking University Health, Wiley Online Library on [03/09/2023]. See the Terms and Conditions (https://onlinelibrary.wiley.com/terms-and-conditions) on Wiley Online Library for rules of use; OA articles are governed by the applicable Creative Commons License

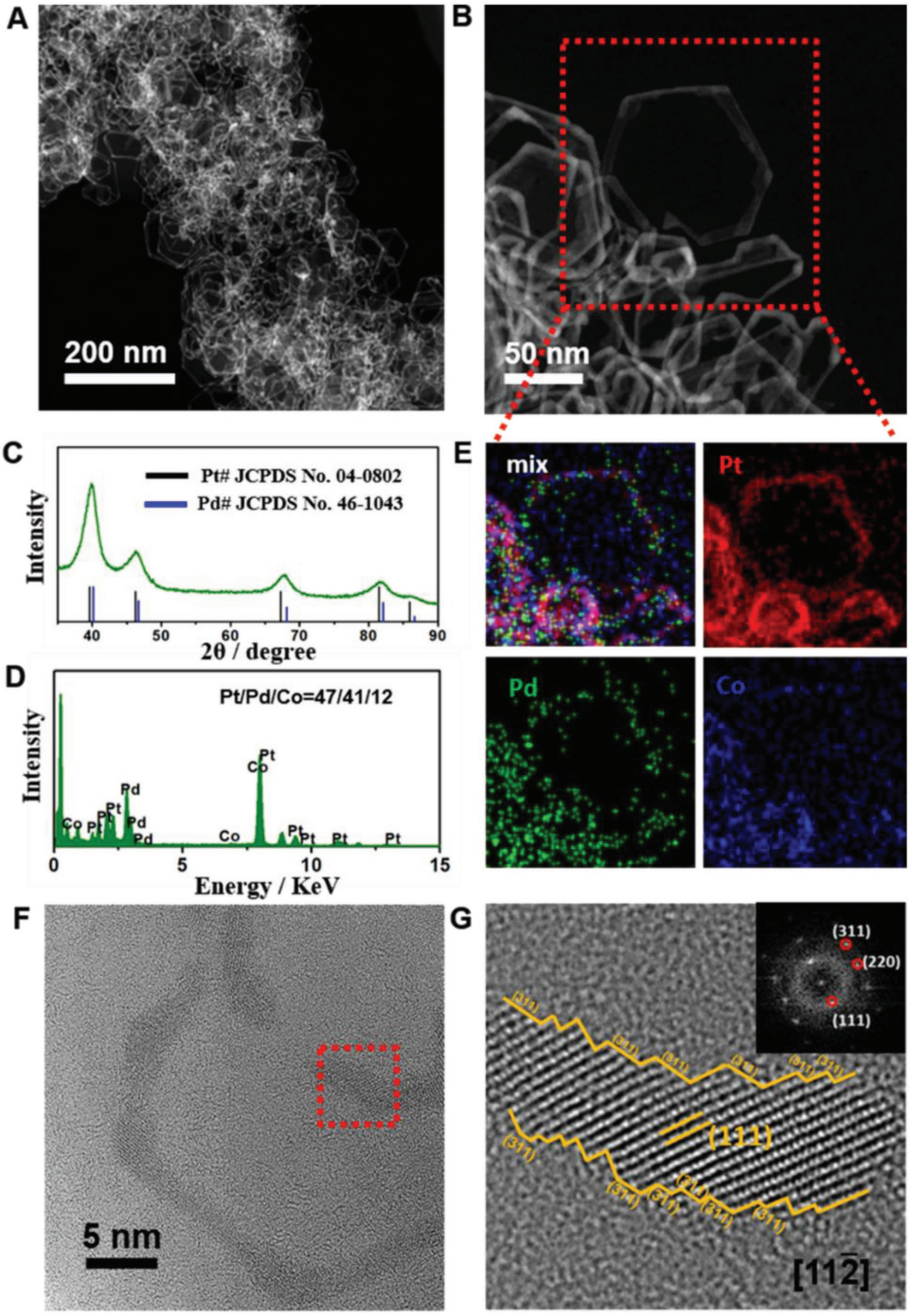

Figure 1. Structure and compositional characterization of PtPdCo NRs. Representative A) low-and B) high-magnification HAADF-STEM images, C) PXRD pattern, D) TEM-EDS, and E) STEM-EDS elemental mapping of PtPdCo NRs. F,G) Typical HRTEM images of an individual PtPdCo NR projected along the zone axes of [112] axis. The inset in panel (G) is FFT pattern of PtPdCo NR.

observed in nanoplates. After 1 h, the hollow interior structure appeared inside the nanoplates (Figure 2C) with the composition at $Pt_{37}Pd_{50}Co_{13}$. Upon continually increasing the reaction time to 5 h, most of the nanoplates were transformed into the NRs (Figure 2D) with the composition at $Pt_{48}Pd_{40}Co_{11}$. Furthermore, with increasing the reaction time, the intermediate products show the shifted XRD peaks (shifting from the peaks attributed to *fcc* Pd phase to those of *fcc* Pt one) (Figure 2F).

To better understand the growth mechanism of the NR, the effects of different experimental parameters on the products were thoroughly investigated, such as metal precursors and surfactants. We found that the $W(CO)_6$ was the indispensable prerequisite to form 2D nanomaterials.

 © 2018 WILEY-VCH Verlag GmbH & Co. KGaA, Weinheim

15214095, 2018, 38, Downloaded from https://onlinelibrary.wiley.com/doi/10.1002/adma.201802136 by Peking University Health, Wiley Online Library on [03/09/2023]. See the Terms and Conditions (https://onlinelibrary.wiley.com/terms-and-conditions) on Wiley Online Library for rules of use; OA articles are governed by the applicable Creative Commons License

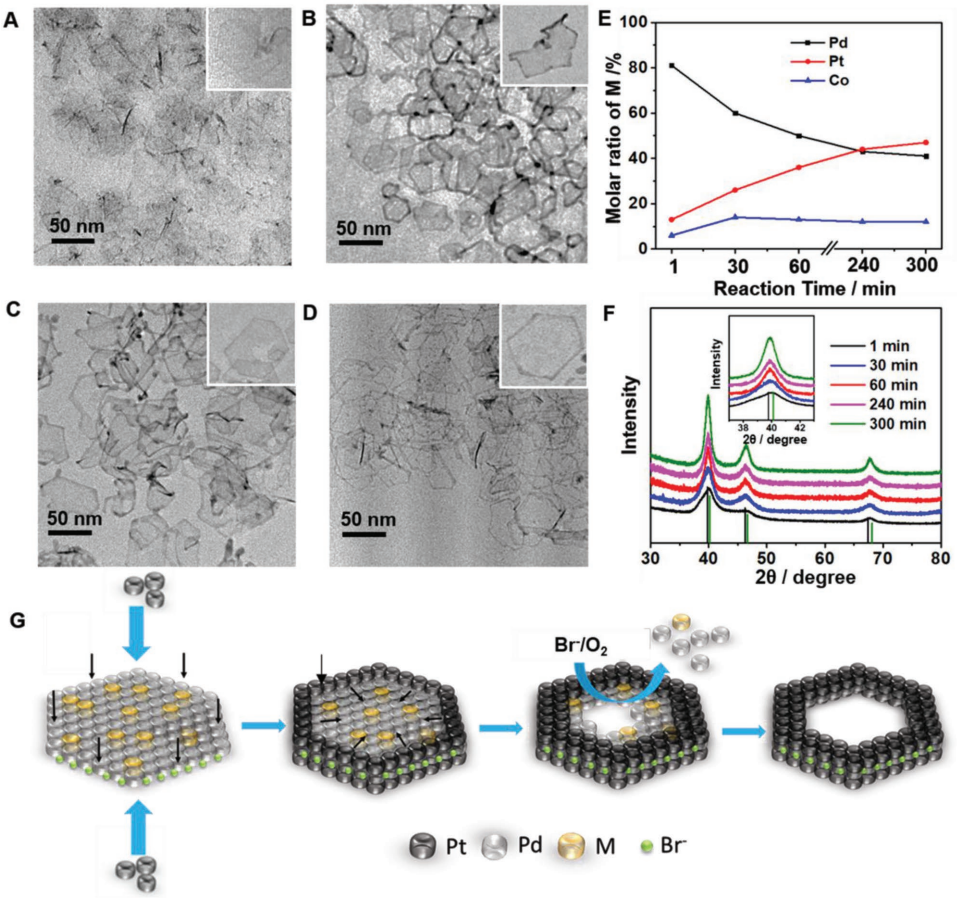

Figure 2. Formation mechanism of PtPdCo NRs. Representative TEM images of PtPdCo NRs intermediates collected from A) 1, B) 30, C) 60, and D) 300 min. E) The changes on the composition ratio of Pt, Pd, and Co for the PtPdCo NRs intermediates, as determined by ICP-AES measurements. F) PXRD patterns of PtPdCo NRs intermediates collected from the reactions at different reaction times. G) The mechanism model of forming a PtPdM (M = Co, Ni, Fe) NR.

Only branched nanocrystals were generated in the absence of $W(CO)_6$ (Figure S9, Supporting Information). When $W(CO)_6$ was replaced with $Mo(CO)_6$, the NRs could still be made (Figure S10, Supporting Information), suggesting that carbonyl group was the important structure-directing agent in producing 2D nanomaterials. The concentration of NH_4Br and the presence of dissolved O_2 were the crucial factors in transforming 2D nanoplates to 2D NRs. There was no NRs appeared when we reduced the amount of NH_4Br (Figure S11, Supporting Information) or conducted the reaction under N_2 atmosphere (Figure S12, Supporting Information), because the O_2 could oxidize and etch the nanoplates from the interior in the presence of Br^-.[34,35] The synthesis of well-fined PtPdCo NRs also highly depended on the ratio of Pt to Pd precursors (Figures S13 and S14, Supporting Information). In particular, the Co composition of the NRs was no longer changed even though the amount of Co precursor was increased (Figure S15, Supporting Information). Therefore, the growth for PtPdCo NRs could probably be divided into three major steps. First, the Pd precursor was quickly reduced with a priority to form the ultrathin PdCo hexagonal nanoplates. Then, PtPdCo nanoplates were obtained because the reduction of moderate amounts of Pt precursor could selectively grow on the periphery of the nanoplates. Finally, the oxidative etching of O_2 in the absence of Br^- plays the important role in making the PtPdCo NRs from the PtPdCo nanoplates (Figure 2G).

The present synthetic strategy was a general method for obtaining different types of 2D PtPdM trimetallic NRs, such as PtPdNi and PtPdFe. The PtPdNi NRs have an average edge length of 26.4 nm and width of 1.51 nm (**Figure 3**A,B and Figure S16, Supporting Information). The HRTEM image of PtPdNi NR exhibits the lattice distance of 0.225 nm, attributed to the (111) plane of the *fcc* Pt or Pd (inset of Figure 3B). The *fcc* crystal phase was confirmed by the PXRD (Figure S17, Supporting Information). The composition of Pt/Pd/Ni n Figure 3C was determined to be 44/43/13 by TEM-EDS (Figure 3C). By replacing the $Ni(acac)_2$ with $Fe(acac)_3$, the PtPdFe NRs with the similar morphology and structure were made, and further characterized by TEM (Figure 3D,E), HRTEM (inset of Figure 2E), PXRD (Figure S17, Supporting Information) and EDS (Figure 3F). The present method could be also used to make the PtPd NRs (Figure S18A,B, Supporting Information) by using the same method except without introducing $M(acac)_x$ as M precursors. The as-made PtPd NRs have an average edge length of 28.7 nm and width of 1.63 nm (Figure S18C, Supporting Information). The space lattice of such PtPd NR, as

© 2018 WILEY-VCH Verlag GmbH & Co. KGaA, Weinheim

15214095, 2018, 38, Downloaded from https://onlinelibrary.wiley.com/doi/10.1002/adma.201802136 by Peking University Health, Wiley Online Library on [03/09/2023]. See the Terms and Conditions (https://onlinelibrary.wiley.com/terms-and-conditions) on Wiley Online Library for rules of use; OA articles are governed by the applicable Creative Commons License

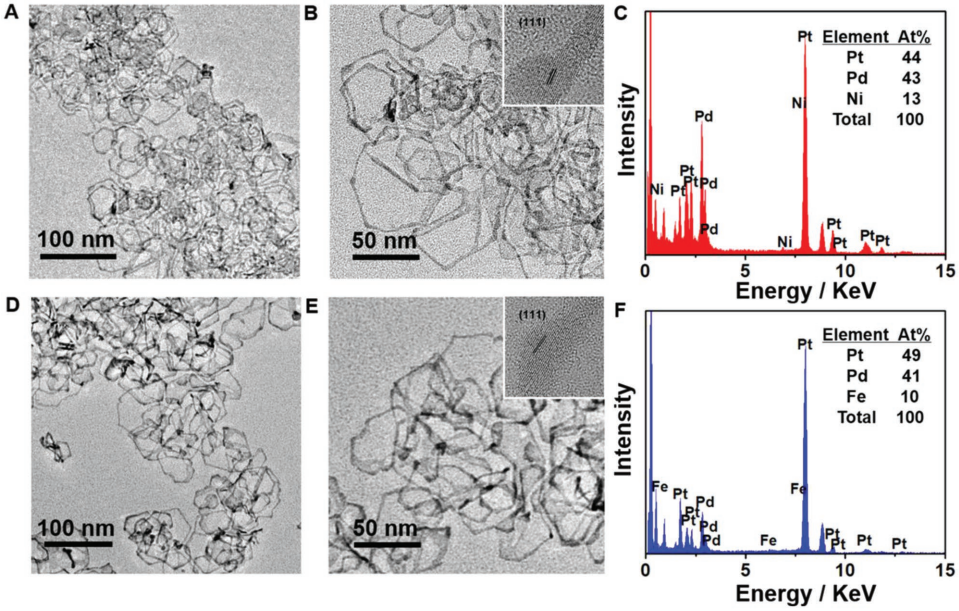

Figure 3. Morphology and structure characterization of PtPdNi and PtPdFe NRs. Representative A,B) TEM images and C) TEM-EDS spectrum of PtPdNi NRs. Representative D,E) TEM images and F) TEM-EDS spectrum of PtPdFe NRs. The insets in panels (B) and (E) are the HRTEM images of PtPdNi NR and PtPdFe NR, respectively.

revealed from HRTEM image, is 0.226 nm, being in agreement with that of PtPd alloys (Figure S18D, Supporting Information). The STEM-EDS elemental mapping demonstrates the uniform distribution of Pt and Pd elements throughout the NRs, confirming their alloying formation (Figure S18E, Supporting Information).

Before the electrochemical measurements, the PtPdCo NRs, PtPdNi NRs, PtPdFe NRs, and PtPd NRs were deposited onto commercial carbon (Vulcan XC72R carbon) support via sonication and then subject to thermal annealing to clean the surface. Figure S19 in the Supporting Information shows the cyclic voltammograms (CVs) of different catalysts at room temperature in a N_2-saturated 0.1 M $HClO_4$ solution at a sweep rate of 50 mV s^{-1}. We evaluated the electrochemical active surface area of each catalysts by integrating the hydrogen adsorption charge ($H^+ + e^- = H_{upd}$) on CV curves (0.05 V < E < 0.35 V). The ORR polarization curves of different catalysts were recorded in an O_2-saturated 0.1 M KOH solution with a rotating rate of 1600 rpm, normalized by geometric area of the RDE (0.196 cm^2) (**Figure** 4A). The half-wave potential ($E_{1/2}$) of PtPdCo NRs/C was 0.966 V versus reversible hydrogen electrode (RHE), higher that those of PtPdNi NRs/C (0.955 V), PtPdFeNRs/C (0.925 V), PtPd NRs/C (0.889 V), and commercial Pt/C (0.849 V) (Figure 4B), indicating obviously enhanced ORR activity for the PtPdCo NRs. Furthermore, the PtPdCo NRs/C exhibits significant improved kinetics relative to PtPd NRs/C and Pt/C (Figure S20, Supporting Information). We also analyze the corresponding SA and MA of the total catalysts at 0.9 V versus RHE (Figure 4C). As expected, the PtPdM NRs/C catalyst exhibits considerable higher activities than that of PtPd NRs/C. Among all PtPd alloy catalysts, the PtPdCo NRs/C catalyst shows the highest specific activity of 4.91 mA cm^{-2}, around 5.5 and 24.5 times higher than those of PtPd NRs/C (0.89 mA cm^{-2}) and Pt/C catalyst (0.21 mA cm^{-2}). The mass activity achieved in the PtPdCo NRs/C was 3.58 A mg^{-1}, higher than PtPdNi NRs/C (2.55 A mg^{-1}), PtPdFe NRs/C (1.04 A mg^{-1}), PtPd NRs/C (0.58 A mg^{-1}), and commercial Pt/C (0.15 A mg^{-1}), suggesting their superior catalytic performance.

We further evaluated the stability of the PtPdCo NRs/C through an accelerated durability test (ADT) under a sweep rate of 500 mV s^{-1} between 0.6 and 1.1 V in O_2-saturated 0.1 M KOH. The ORR polarization curves (Figure 4D) of PtPdCo NRs/C before and after 30 000 CV cycles show little change in mass activity by dropping only 29%, in contrast to that of Pt/C catalyst (72.5%) (Figure S21, Supporting Information), indicating the superior stability of PtPdCo NRs, which was further proved by the fact that the PtPdCo NRs/C showed the negligible change of the structure before and after ADT (Figure S22, Supporting Information). The good durability can be also confirmed by the PtPdCo NRs shows the slower current decay than Pt/C catalyst in the chronoamperometric response (Figure S23, Supporting Information). The PtPdCo NRs/C also shows the highest specific and mass activities of 1.26 mA cm^{-2} and 0.92 A mg^{-1} at 0.9 V versus RHE in acid solutions, 2.1 and 2.4 times, and 4.5 and 6.1 times higher than those of PtPd NRs/C and commercial Pt/C, respectively (Figure S24, Supporting Information).

The high ORR activity of PtPdM NRs can be attributed to their maximized explosion of Pt atoms due to their ultrathin nature and also the optimized adsorptive behavior of stepped atoms for oxygen species. To further shed light on the exceptional ORR performance of the PtPdM NRs (take PtPdCo as example), we employed DFT to analyze the oxygen adsorption energy (E_O), an excellent descriptor for ORR activity.[36,37] There exists an optimal E_O value under which the ORR activity of the catalyst reaches the maximum. It turns out that Pt–O bonding on a perfect Pt (111) surface is 0.2 eV stronger than the optimal level.[36,37] For convenience, we shifted the optimal

© 2018 WILEY-VCH Verlag GmbH & Co. KGaA, Weinheim

15214095, 2018, 38, Downloaded from https://onlinelibrary.wiley.com/doi/10.1002/adma.201802136 by Peking University Health, Wiley Online Library on [03/09/2023]. See the Terms and Conditions (https://onlinelibrary.wiley.com/terms-and-conditions) on Wiley Online Library for rules of use; OA articles are governed by the applicable Creative Commons License

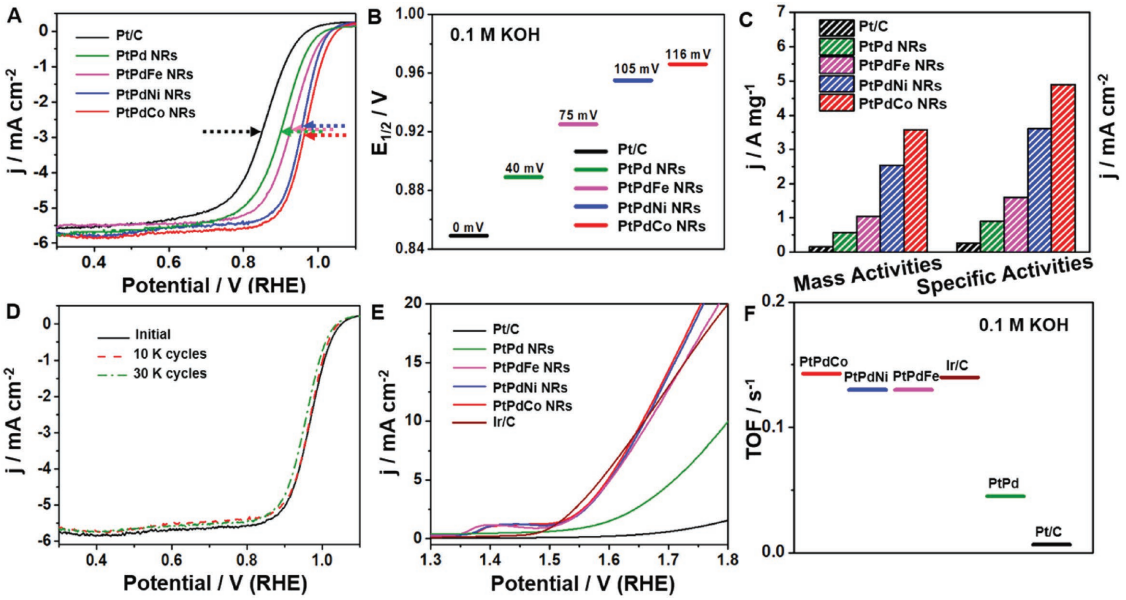

Figure 4. Electrocatalytic performance of PtPdCo NRs/C, PtPdNi NRs/C, PtPdFe NRs/C, PtPd NRs/C, and commercial Pt/C. A) ORR polarization curves, B) half-wave potential ($E_{1/2}$) values, C) histogram of MA and SA of different catalysts. Polarization curves were recorded at room temperature in an O_2-saturated KOH aqueous solution at a sweep rate of 20 mV s^{-1} and a rotation rate of 1600 rpm. D) ORR polarization curves before and after 10 000 and 30 000 potential cycles between 0.6 and 1.1 V versus RHE. E) OER polarization curves and F) TOF values of different catalysts. Current densities of OER normalized to the total mass of PtPdM, and the values are calculated from the current at overpotential of 300 mV.

E_O value to 0 eV and use ΔE_O to represent the difference of a given E_O value relative to this optimal reference. Thus, a surface with ΔE_O value closer to zero (the smaller length of the bar in **Figure 5**) is believed to exhibit a superior ORR activity. Considering the observation that (111) and (311) facets dominate the surfaces of NRs, we then focus on these two facets. To simplify calculations, we focus on the intermetallic PtPd surfaces. On the (111) flat surface, we determine E_O for oxygen adsorbed at two inequivalent *fcc* hollow sites (H). On the (311) stepped surface, three typical adsorption sites were examined-one bridge site (B) at the edge and two hollow sites (H) on the facet. As a comparison, we also calculated the ΔE_o on both the "bridge" and "hollow" sites of a Pt nanoparticle with the diameter of 3.5 nm following Ref. [38] The values of ΔE_O on the PtPd (111) and (311) surfaces are shown in Figure 5, ΔE_O on the PtPd (111) surface is more negative than that on the Pt (111) facet since oxygen overbinds to Pd. On the PtPd (311) surface, ΔE_O is closer to the optimal energy than that of the Pt NP, thus a higher ORR activity on the (311) surface is expected. Therefore, the presence of step atoms on the PtPd

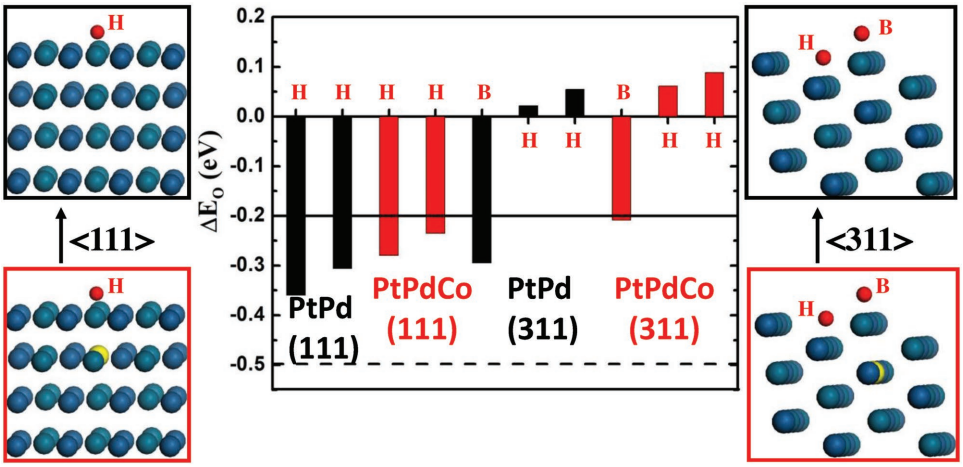

Figure 5. DFT calculation of oxygen adsorption energy. ΔE_O on the PtPd and PtPdCo (111) and (311) surfaces. The black and red bars represent PtPd and PtPdCo, respectively. "H" and "B" indicate that the O atom is adsorbed on the *fcc* hollow site of the facet and the bridge site of the edge, respectively. There are two inequivalent hollow sites on both the (111) and (311) surfaces. The blue, green, yellow, and red spheres represent Pt, Pd, Co, and O atoms, respectively. The solid and dashed horizontal lines represent ΔE_O values on the *fcc* hollow site of the (111) facet and the bridge site of the edge of a cuboctahedra Pt nanoparticle with a diameter of 3.5 nm.

 © 2018 WILEY-VCH Verlag GmbH & Co. KGaA, Weinheim

15214095, 2018, 38, Downloaded from https://onlinelibrary.wiley.com/doi/10.1002/adma.201802136 by Peking University Health, Wiley Online Library on [03/09/2023]. See the Terms and Conditions (https://onlinelibrary.wiley.com/terms-and-conditions) on Wiley Online Library for rules of use; OA articles are governed by the applicable Creative Commons License

NRs enhances the ORR performance, in consistent with the experimental observation.

By introducing Co into PtPd, in general both surface strain and ligand effect induced by the Co atoms can influence their catalytic activities for ORR. However, the strain effect should not be noticeable due to the low concentration of Co (≈12%) in the PtPdCo NRs. Here, we focus on the ligand effect, which might significantly alter the ORR performance. Since the ligand effect of Co in the deeper layers on the ΔE_o can be negligible, here we only consider the presence of Co in the subsurface layer. To this end, we model the PtPdCo surfaces by substituting a Pd atom with a Co atom in the subsurface layer, corresponding to a 12.5% concentration of Co. ΔE_O on the PtPdCo surface was evaluated at the adsorption sites, which are adjacent to the Co atom, and was contrasted to that on the PtPd surface. The presence of Co reduces the binding between the oxygen and PtPd on both (111) and (311) surfaces. On the (311) surface, the Pt-O binding is much weaker on the "hollow" sites than their adjacent "bridge" sites, as shown in Figure 5, and the diffusion barrier is less than 0.05 eV from a "hollow" site to a "bridge" site. Thus, the "hollow" sites did not contribute meaningfully to the overall ORR; however, the "bridge" site will be dominant. The ligand effect of Co could release the Pt-O overbinding on the "bridge" sites of (311) surfaces, thus improving the ORR performance. More specifically, the step atoms on (311) edge become active with the similar ORR performance as that of the Pt (111) facet. These results imply that the PtPdCo NRs should have higher ORR activities than the PtPd NRs.

The different NRs were also studied for OER in O_2-saturated 0.1 M KOH solution at scan rate of 5 mV s^{-1}. Normally, the Pt-based catalysts were not very active to OER. Herein, the PtPdM NRs, however, exhibit an excellent activity toward OER. The polarization curves in Figure 4E reveal that all PtPdM NRs have the anodic peak at around 1.4 V versus RHE, attributed to the oxidation processes of Co^{2+}/Co^{3+}, Ni^{2+}/Ni^{3+} and Fe^{2+}/Fe^{3+}.[39] The PtPdM NRs show the onset potential of ≈1.5 V, close to commercial Ir/C (1.47 V), much lower than those of PtPd NRs (≈1.62 V) and Pt/C (≈1.7 V). The TOF of different catalysts (normalizing current densities to active sites of catalysts at an overpotential of 300 mV) was calculated to further evaluate the intrinsic activity of catalysts (Figure 4F). The TOF of PtPdCo NRs reaches 0.14 s^{-1}, 3.1, and 21.5 times higher than those of PtPd NRs (0.045 s^{-1}) and Pt/C (0.0065 s^{-1}). The OER performances of different NRs catalysts follow the order of PtPdCo NRs > PtPdNi NRs ≈PtPdFe NRs > PtPd NRs, indicating the important role of Co/Ni/Fe in the PtPdM catalysts. The enhanced OER performance of PtPdM NRs was probably caused by a little bit of Ni, Co, Fe oxyhydroxides/oxides on the surface of NRs that were formed by the oxidation of Ni, Co, and Fe surface atoms.[40–42]

To summarize, we demonstrate a universal method for making 2D alloyed multimetallic PtPdM (M = Co, Ni, Fe) NRs as remarkable bifunctional catalysts for ORR and OER. Time-dependent measurements reveal that the formation of unique nanorings configuration critically relies on the initial formation of 2D PdM nanoplates, the reduction of Pt onto the side of nanoplates, and the oxidation etching by O_2 in the presence of Br^-. The ultrathin NRs feature with high atom utilization, numerous step atoms on edge, heteroatomic alloying and unique 2D ring geometric structure, making them exhibit the highest mass and specific activities for ORR in alkaline condition, 23.9- and 24.5-fold enhancement relative to those of Pt/C, respectively. The DFT studies indicate that the step atom and ligand effects can optimize the oxygen adsorption energy (E_O), thereby a superior ORR performance. Moreover, the PtPdCo NRs/C is very stable for ORR with a drop of only 29% in mass activity after 30 000 ADT cycling tests, much lower than that of benchmark Pt/C catalyst (a big decrease of 72.5%). Especially, the PtPdM NRs also display good OER performance with an onset potential of ≈1.5 V versus RHE, better than those of PtPd NRs and Pt/C. This work highlights a general strategy to obtain a novel PtPdM NR structures at atomic level with excellent bifunctional electrocatalytic performance for ORR and OER. We believe that the achievement of the production of such interesting NR structures will open new horizons toward the rational design of more efficient relevant catalysts for regenerative fuel cells, metal-O_2 batteries, and beyond.

Supporting Information

Supporting Information is available from the Wiley Online Library or from the author.

Acknowledgements

This work was financially supported by the National Natural Science Foundation of China (NSFC) (No. 51671003), National Basic Research Program of China (No. 2017YFA0206701), the China Postdoctoral Science Foundation (No. 2017M610022), Open Project Foundation of State Key Laboratory of Chemical Resource Engineering, the start-up supports from Peking University and Young Thousand Talented Program. The work at California State University Northridge was supported by the Office of Naval Research (N00014-15-1-2092) and National Science Foundation (DMR-1205734). The authors acknowledge Electron Microscopy Laboratory in Peking University for the use of Cs corrected electron microscope.

Conflict of Interest

The authors declare no conflict of interest.

Keywords

fuel cells, multimetallic, nanorings, oxygen reduction, step atoms

Received: April 3, 2018
Revised: June 22, 2018
Published online: August 6, 2018

[1] M. K. Debe, *Nature* **2012**, *486*, 43.
[2] H. A. Gasteiger, N. M. Markovic, *Science* **2009**, *324*, 48.
[3] O. Gröger, H. A. Gasteiger, J.-P. Suchsland, *J. Electrochem. Soc.* **2015**, *162*, A2605.

© 2018 WILEY-VCH Verlag GmbH & Co. KGaA, Weinheim

15214095, 2018, 38, Downloaded from https://onlinelibrary.wiley.com/doi/10.1002/adma.201802136 by Peking University Health, Wiley Online Library on [03/09/2023]. See the Terms and Conditions (https://onlinelibrary.wiley.com/terms-and-conditions) on Wiley Online Library for rules of use; OA articles are governed by the applicable Creative Commons License

[4] H. A. Gasteiger, S. S. Kocha, B. Sompalli, F. T. Wagner, *Appl. Catal. B: Environ.* **2005**, *56*, 9.
[5] M. Luo, Y. Sun, L. Wang, S. Guo, *Adv. Energy. Mater.* **2017**, *7*, 1602073.
[6] M. Oezaslan, F. Hasché, P. Strasser, *J. Phys. Chem. Lett.* **2013**, *4*, 3273.
[7] Y. Xia, X. Yang, *Acc. Chem. Res.* **2017**, *50*, 450.
[8] Z. W. Seh, J. Kibsgaard, C. F. Dickens, I. Chorkendorff, J. K. Norskov, T. F. Jaramillo, *Science* **2017**, *355*, 6321.
[9] Y. Jiao, Y. Zheng, M. Jaroniec, S. Z. Qiao, *Chem. Soc. Rev.* **2015**, *44*, 2060.
[10] M. Luo, S. Guo, *Nat. Rev. Mater.* **2017**, *2*, 17059.
[11] M. Shao, Q. Chang, J. P. Dodelet, R. Chenitz, *Chem. Rev.* **2016**, *116*, 3594.
[12] I. E. L. Stephens, A. S. Bondarenko, U. Grønbjerg, J. Rossmeisl, I. Chorkendorff, *Energy Environ. Sci.* **2012**, *5*, 6744.
[13] P. Strasser, S. Kühl, *Nano Energy* **2016**, *29*, 166.
[14] Z. Y. Zhou, N. Tian, J. T. Li, I. Broadwell, S. G. Sun, *Chem. Soc. Rev.* **2011**, *40*, 4167.
[15] V. R. Stamenkovic, D. Strmcnik, P. P. Lopes, N. M. Markovic, *Nat. Mater.* **2016**, *16*, 57.
[16] H. Mistry, A. S. Varela, S. Kühl, P. Strasser, B. R. Cuenya, *Nat. Rev. Mater.* **2016**, *1*, 16009.
[17] M. Luo, Y. Sun, X. Zhang, Y. Qin, M. Li, Y. Li, C. Li, Y. Yang, L. Wang, P. Gao, G. Lu, S. Guo, *Adv. Mater.* **2018**, *30*, 1705515.
[18] N. Becknell, Y. Son, D. Kim, D. Li, Y. Yu, Z. Niu, T. Lei, B. T. Sneed, K. L. More, N. M. Markovic, V. R. Stamenkovic, P. Yang, *J. Am. Chem. Soc.* **2017**, *139*, 11678.
[19] T. Sheng, N. Tian, Z.-Y. Zhou, W.-F. Lin, S.-G. Sun, *ACS Energy Lett.* **2017**, *2*, 1892.
[20] B. P. Setzler, Z. Zhuang, J. A. Wittkopf, Y. Yan, *Nat. Nanotechnol.* **2016**, *11*, 1020.
[21] H. Zhang, *ACS Nano* **2015**, *9*, 9451.
[22] C. Tan, X. Cao, X. J. Wu, Q. He, J. Yang, X. Zhang, J. Chen, W. Zhao, S. Han, G. H. Nam, M. Sindoro, H. Zhang, *Chem. Rev.* **2017**, *117*, 6225.
[23] D. Deng, K. S. Novoselov, Q. Fu, N. Zheng, Z. Tian, X. Bao, *Nat. Nanotechnol.* **2016**, *11*, 218.
[24] X. Huang, S. Tang, X. Mu, Y. Dai, G. Chen, Z. Zhou, F. Ruan, Z. Yang, N. Zheng, *Nat. Nanotechnol.* **2011**, *6*, 28.
[25] C. Hu, Q. Ma, S.-F. Hung, Z.-N. Chen, D. Ou, B. Ren, H. M. Chen, G. Fu, N. Zheng, *Chem* **2017**, *3*, 122.
[26] H. Liu, P. Zhong, K. Liu, L. Han, H. Zheng, Y. Yin, C. Gao, *Chem. Sci.* **2018**, *9*, 398.
[27] X. Zhao, L. Dai, Q. Qin, F. Pei, C. Hu, N. Zheng, *Small* **2017**, *13*.
[28] F. Salaam, B. Xu, B. Ni, H. Liu, F. Nosheen, H. Li, X. Wang, *Adv. Mater.* **2015**, *27*, 2013.
[29] Y. Kang, Q. Xue, P. Jin, J. Jiang, J. Zeng, Y. Chen, *ACS Sustainable Chem. Eng.* **2017**, *5*, 10156.
[30] S. Gao, Y. Lin, X. Jiao, Y. Sun, Q. Luo, W. Zhang, D. Li, J. Yang, Y. Xie, *Nature* **2016**, *529*, 68.
[31] L. Bu, J. Ding, S. Guo, X. Zhang, D. Su, X. Zhu, J. Yao, J. Guo, G. Lu, X. Huang, *Adv. Mater.* **2015**, *27*, 7204.
[32] S. Jiang, Y. Ma, G. Jian, H. Tao, X. Wang, Y. Fan, Y. Lu, Z. Hu, Y. Chen, *Adv. Mater.* **2009**, *21*, 4953.
[33] L. Bu, S. Guo, X. Zhang, X. Shen, D. Su, G. Lu, X. Zhu, J. Yao, J. Guo, X. Huang, *Nat. Commun.* **2016**, *7*, 11850.
[34] Y. Li, W. Wang, K. Xia, W. Zhang, Y. Jiang, Y. Zeng, H. Zhang, C. Jin, Z. Zhang, D. Yang, *Small* **2015**, *11*, 4745.
[35] E. White, S. Singer, V. Augustyn, W. Hubbard, M. Mecklenburg, B. Dunn, B. Regan, *ACS Nano* **2012**, *6*, 6308.
[36] J. K. Nørskov, J. Rossmeisl, A. Logadottir, L. Lindqvist, J. R. Kitchin, T. Bligaard, H. Jónsson, *J. Phys. Chem. B* **2004**, *108*, 17886.
[37] V. Stamenkovic, B. S. Mun, K. J. Mayrhofer, P. N. Ross, N. M. Markovic, J. Rossmeisl, J. Greeley, J. K. Nørskov, *Angew. Chem., Int. Ed.* **2006**, *118*, 2963.
[38] L. Li, A. Larsen, N. Romero, V. Morozov, C. Glinsvad, F. Abild-Pedersen, J. Greeley, K. Jacobsen, J. Nørskov, *J. Phys. Chem. Lett.* **2013**, *4*, 222.
[39] L. Qian, Z. Lu, T. Xu, X. Wu, Y. Tian, Y. Li, Z. Huo, X. Sun, X. Duan, *Adv. Energy Mater.* **2015**, *6*, 1500245.
[40] K. Xu, P. Chen, X. Li, Y. Tong, H. Ding, X. Wu, W. Chu, Z. Peng, C. Wu, Y. Xie, *J. Am. Chem. Soc.* **2015**, *137*, 4119.
[41] K. Xu, H. Ding, H. Lv, P. Chen, X. Lu, H. Cheng, T. Zhou, S. Liu, X. Wu, C. Wu, Y. Xie, *Adv. Mater.* **2016**, *28*, 3326.
[42] L. Stern, L. Feng, F. Song, X. Hu, *Energy Environ. Sci.*, **2015**, *8*, 2347.

© 2018 WILEY-VCH Verlag GmbH & Co. KGaA, Weinheim

15214095, 2018, 38, Downloaded from https://onlinelibrary.wiley.com/doi/10.1002/adma.201802136 by Peking University Health, Wiley Online Library on [03/09/2023]. See the Terms and Conditions (https://onlinelibrary.wiley.com/terms-and-conditions) on Wiley Online Library for rules of use; OA articles are governed by the applicable Creative Commons License